Toyokuni and Zhao
Progress in Earth and Planetary Science (2023) 10:64
https://doi.org/10.1186/s40645-023-00595-7

Progress in Earth and Planetary Science

RESEARCH ARTICLE

Open Access

Ancient slabs beneath Arctic and surroundings: Izanagi, Farallon, and in-betweens

Genti Toyokuni[1*] and Dapeng Zhao[1]

Abstract

A detailed 3-D tomographic model of the whole mantle beneath the northern hemisphere (north of ~ 30°N latitude) is obtained by inverting a large amount of *P*-wave arrival time data (*P*, *pP*, and *PP*) to investigate transition of subducted slabs beneath Eurasia–Arctic–North America. We apply an updated global tomographic method that can investigate the whole mantle 3-D structure beneath a target area with high resolution comparable to that of regional tomography. The final tomographic model is obtained by performing independent calculations for 12 different target areas and stitching together the results. Our model clearly shows the subducted Izanagi and Farallon slabs penetrating into the lower mantle beneath Eurasia and North America, respectively. In the region from Canada to Greenland, a stagnant slab lying below the 660-km discontinuity is revealed. Because this slab has a texture that seems to be due to subducted oceanic ridges, the slab might be composed of the Farallon and Kula slabs that had subducted during ~60–50 Ma. During that period, a complex rift system represented by division between Canada and Greenland was developed. The oceanic ridge subduction and hot upwelling in the big mantle wedge above the stagnant slab caused a tensional stress field, which might have induced these complex tectonic events.

Keywords Seismic tomography, Arctic region, Subducting slab, Subduction zone, Big mantle wedge (BMW), Izanagi slab, Farallon slab

1 Introduction

The underground structure beneath the circum-Arctic region (Fig. 1) is a frontier of our geoscientific knowledge, which is poorly understood compared to other regions of the northern hemisphere. Especially in recent years, the underground structure and tectonics of this region have received wide attentions because, for example, a possibility of resource mining has increased due to decrease in ice in the Arctic Ocean, and the underground temperature affects melting of the Greenland Ice Sheet and global sea level rise (Martos et al. 2018; Toyokuni et al. 2020a).

The slabs that have subducted into the mantle may affect the evolution of the Earth's surface. Especially in the northern hemisphere, the Farallon and Izanagi slabs, which had subducted for a long time, are considered to have a decisive impact (Fig. 2). Recent studies have suggested that the Mid-Atlantic Ridge (MAR) in the northern hemisphere was opened by hot mantle return-flow when the Farallon slab beneath North America sank into the lower mantle (e.g., Dal Zilio 2018; Dal Zilio et al. 2018). The Farallon slab beneath North America has been revealed by many previous studies using seismic

*Correspondence:
Genti Toyokuni
toyokuni@tohoku.ac.jp
[1] Department of Geophysics, Graduate School of Science, Tohoku University, Sendai 980-8578, Japan

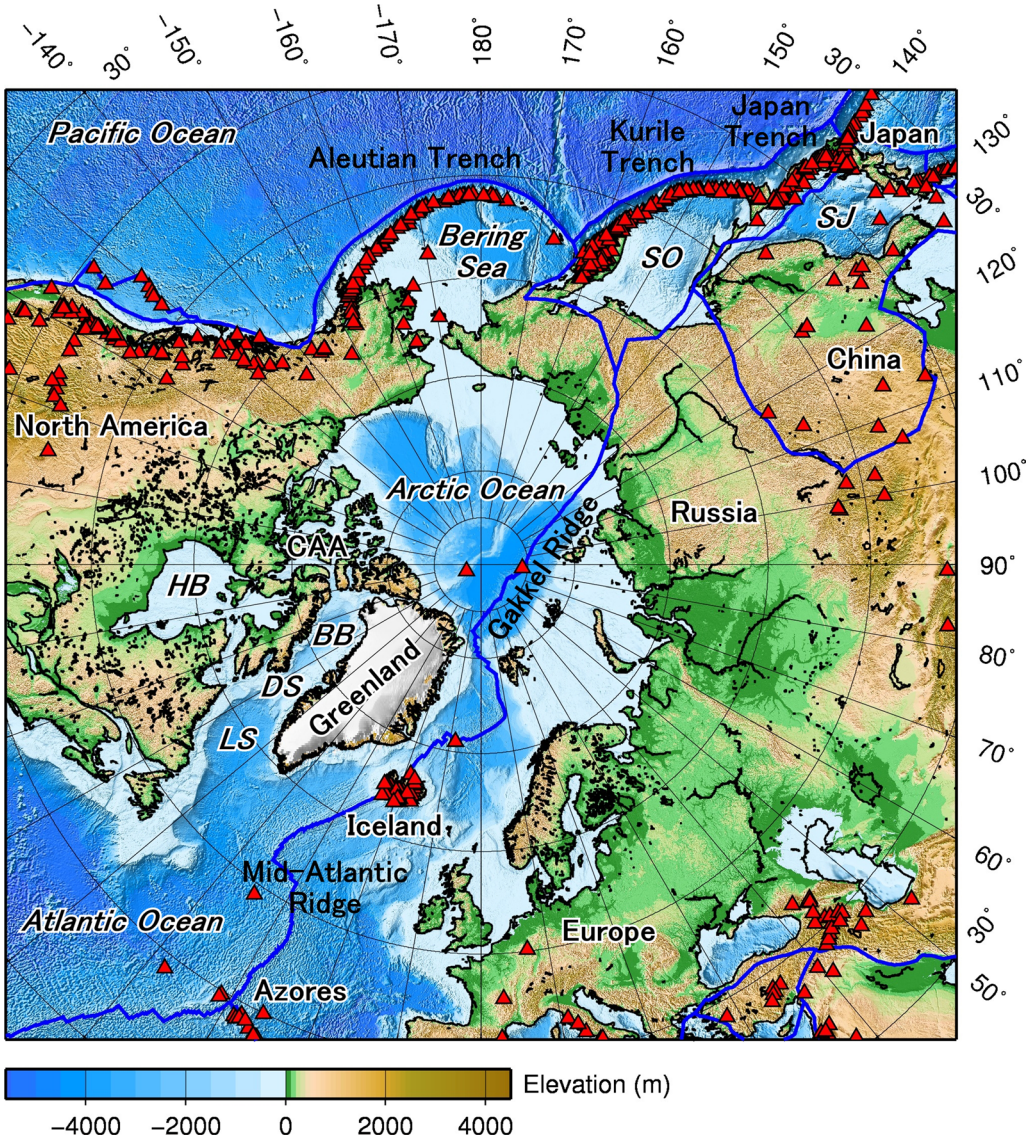

Fig. 1 Map of the circum-Arctic region. The color scale for the topography is shown at the bottom. White color denotes the Greenland Ice Sheet. Red triangles: active volcanoes; thick blue lines: plate boundaries. CAA = Canadian Arctic Archipelago; BB = Baffin Bay; DS = Davis Strait; HB = Hudson Bay; LS = Labrador Sea; SJ = Sea of Japan; SO = Sea of Okhotsk

tomography (e.g., Grand et al. 1997; Schmid et al. 2002; Zhao 2004; Zhao et al. 2013), but the subducted Izanagi slab beneath Eurasia is still poorly understood.

One of the major mysteries of tectonics in the circum-Arctic region is the existence of the Canadian Arctic rift system (CARS). Its latest activity was the Eurekan rifting episode (ERE), symbolized by the division between Greenland and Canada and complex movement of the Canadian Arctic Archipelago (CAA), which took place between 63 and 35 Ma (Gion et al. 2017) (Fig. 2c). It is known that this division began in the Labrador Sea on the southern side and propagated to Baffin Bay on the northern side. Simultaneously, flood basalts erupted widely in West Greenland, Davis Strait, and Baffin Island (Chalmers et al. 1995; Larsen et al. 2016). Traditionally, these events were thought to be induced by the rising Iceland plume (Gerlings et al. 2009; Gill et al. 1992). However, reconstruction of the plume track (Peace et al. 2017), geothermal heat flow estimation (Artemieva 2019; Martos et al. 2018), and seismic velocity structure (Toyokuni et al. 2020a) suggest that it is unlikely that the Iceland plume passed through this area. Peace et al.

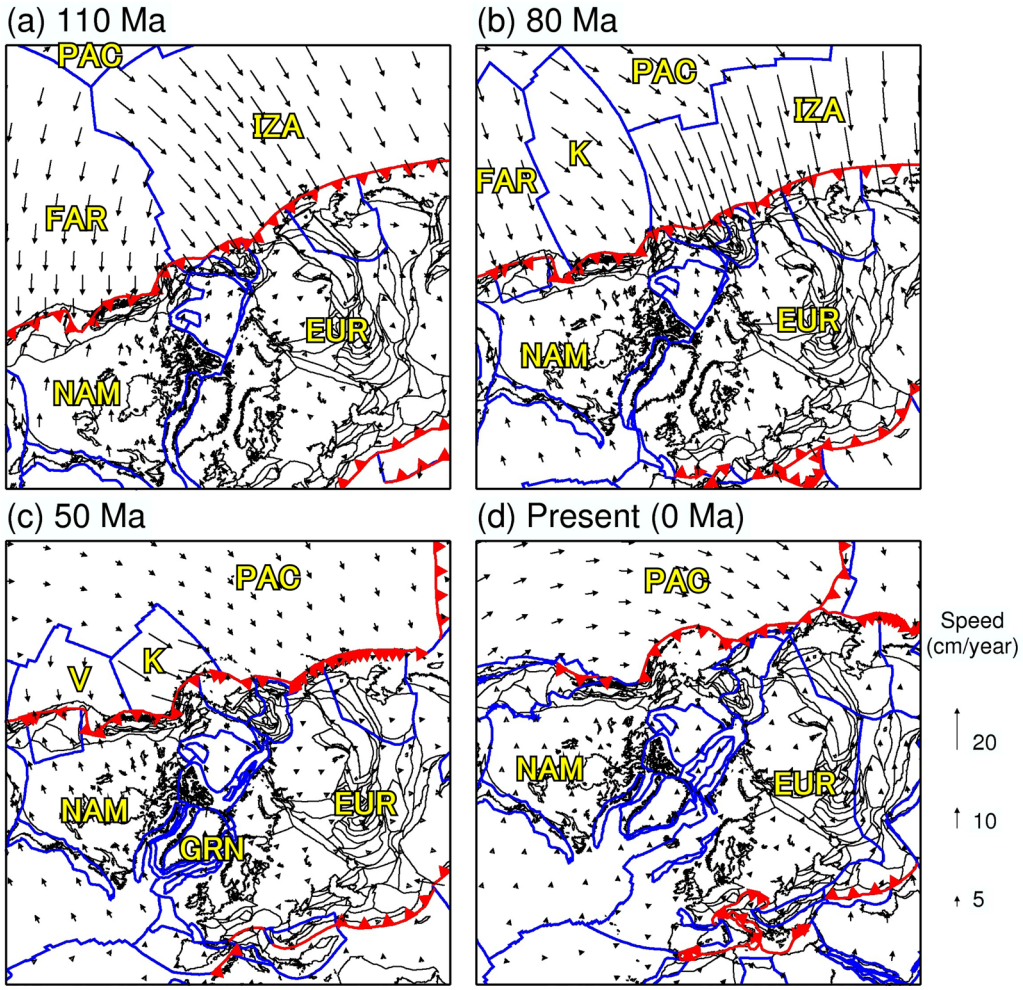

Fig. 2 Past plate positions estimated by the plate reconstruction (Müller et al. 2019). The age of reconstruction is shown above each panel. Red jagged lines delineate subduction zones, and blue lines denote mid-ocean ridges and transform faults. The length and azimuth of each arrow denote the rate and direction of the absolute plate motion, respectively. The scale for the plate motion rate is shown on the right. EUR = Eurasian Plate; FAR = Farallon Plate; GRN = Greenland Plate; IZA = Izanagi Plate; K = Kula Plate; NAM = North American Plate; PAC = Pacific Plate; V = Vancouver Plate

(2017) proposed that a far-field tectonic force caused the division, but they did not mention what the force is. During that period, some smaller plates, e.g., the Kula and Vancouver plates (Fig. 2c) as well as oceanic ridges in-betweens, might have also subducted, so their roles should be also considered.

In Greenland, a seismograph network has recently been installed with international cooperation, and high-quality data have been accumulated (Clinton et al. 2014; Toyokuni et al. 2014). The underground structures beneath Greenland, Iceland, and surrounding regions have been extensively investigated by seismic waveform analyses (Kumar et al. 2007; Mordret et al. 2016; Toyokuni et al. 2015, 2018, 2021a), surface wave tomography (Antonijevic and Lees 2018; Darbyshire et al. 2004, 2018; Levshin et al. 2017; Mordret 2018; Pilidou et al. 2004; Pourpoint et al. 2018), body wave tomography (Toyokuni and Zhao 2021; Toyokuni et al. 2020a, b), and full-wave tomography (Rickers et al. 2013). Although several previous studies targeted the whole circum-Arctic region, these only focused on the structure shallower than 700 km depth (Jakovlev et al. 2012; Lebedev et al. 2018). Seismic tomography, especially body-wave tomography, is a well-established high-resolution method for investigating the 3-D mantle structure of the Earth. To investigate the relationship between tectonics of the

circum-Arctic region and large-scale geodynamic events such as plate subduction and hot mantle plumes that occurred or are occurring in or around the Arctic region, we need to study the whole mantle structure with high resolution over a vast horizontal scale. In this study we exploit the updated global tomography method that can reveal the whole mantle *P*-wave velocity (V_P) structure beneath a specific area with high resolution (Toyokuni et al. 2020b; Zhao et al. 2017) to execute multiple computations for different areas, and to obtain detailed panoramic tomography by stitching the individual images together. The purpose of this study is to obtain robust images of the Izanagi, Farallon and other possible slabs in this region, to investigate their relationships, and to infer the cause of ERE from a tectonic viewpoint using our novel tomographic model.

2 Data and method

We apply the multiscale global tomography method by Zhao et al. (2017), which adopts a fine 3-D grid for the target region and a coarse 3-D grid for the surrounding regions of the globe. Thus, the 3-D velocity model beneath the target region can be obtained with high resolution while saving computational resources. Applying this method to the Izu-Bonin subduction zone, Zhao et al. (2017) investigated the detailed 3-D structure of the subducted Pacific slab where the 2015 Bonin deep earthquake (M7.9; ~670 km depth) took place. This method was also applied to investigate the whole mantle structure beneath Greenland (Toyokuni et al. 2020b), the South China Sea (Zhao et al. 2021), and Southeast Asia (Toyokuni et al. 2022).

We apply a coordinate transformation technique to move the center of the target area to the equator (longitude = 90°, latitude = 0°) to treat high latitude areas with a nearly rectangular grid distribution (Takenaka et al. 2017; Toyokuni et al. 2020a, b). To clarify the relationship between tectonic features with a large horizontal scale such as plate subduction and hot mantle upwelling, our target covers the entire region north of ~ 30°N latitude. The computational cost is reduced by performing independent calculations with 12 different regions and superimposing the results to obtain a final tomographic model.

Table 1 shows the central location (longitude and latitude) of each of the 12 regions. Each calculation is performed for a region covering the longitude range from 60°

Table 1 Information on the tomographic inversions for the 12 regions

Region	Center (lon, lat)	Block size	$N_{station}$ (in)	$N_{station}$ (total)	N_{event}	N_P	N_{pP}	N_{PP}	N_{total}
1	(0.0, 90.0)	0.1°×5.0 km (in) 1.0°×20.0 km (out)	923	12,543	17,827	5,762,140	188,989	128,476	6,079,605
2	(−38.461, 90.0)	0.1°×5.0 km (in) 1.0°×20.0 km (out)	1295	12,640	19,045	6,084,018	196,719	130,135	6,410,872
3	(−100.0, 60.0)	0.1°×5.0 km (in) 1.0°×20.0 km (out)	4164	12,612	17,671	5,738,009	190,145	129,393	6,057,547
4	(110.0, 50.0)	0.7°×10.0 km (in) 1.3°×20.0 km (out)	1183	12,485	16,033	5,623,441	183,447	122,100	5,928,988
5	(80.0, 60.0)	0.2°×10.0 km (in) 1.0°×20.0 km (out)	1028	12,555	19,288	6,006,788	197,460	131,146	6,335,394
6	(−70.0, 50.0)	0.1°×5.0 km (in) 1.0°×20.0 km (out)	2469	12,565	17,167	5,658,950	178,360	127,522	5,964,832
7	(−120.0, 35.0)	0.1°×5.0 km (in) 1.0°×20.0 km (out)	3618	12,612	19,817	6,190,973	206,735	134,798	6,532,506
8	(−170.0, 40.0)	0.3°×10.0 km (in) 1.0°×20.0 km (out)	705	12,659	19,515	6,448,371	209,746	134,384	6,792,501
9	(150.0, 35.0)	0.7°×10.0 km (in) 1.3°×20.0 km (out)	1021	12,611	17,150	5,907,332	186,988	127,138	6,221,458
10	(60.0, 35.0)	0.3°×10.0 km (in) 1.0°×20.0 km (out)	2307	12,551	19,120	5,974,579	198,425	131,238	6,304,242
11	(10.0, 40.0)	0.1°×5.0 km (in) 1.0°×20.0 km (out)	3863	12,558	19,078	5,919,055	187,066	129,807	6,235,928
12	(−30.0, 35.0)	0.1°×5.0 km (in) 1.0°×20.0 km (out)	1687	12,542	17,276	5,664,954	178,391	126,679	5,970,024

(in): inside the target volume; (out): outside the target volume; $N_{station}$: the number of stations; N_{event}: the number of seismic events; N_P, N_{pP}, and N_{PP}: the number of arrival times for *P*, *pP*, and *PP* waves; N_{total}: the total number of arrival times used

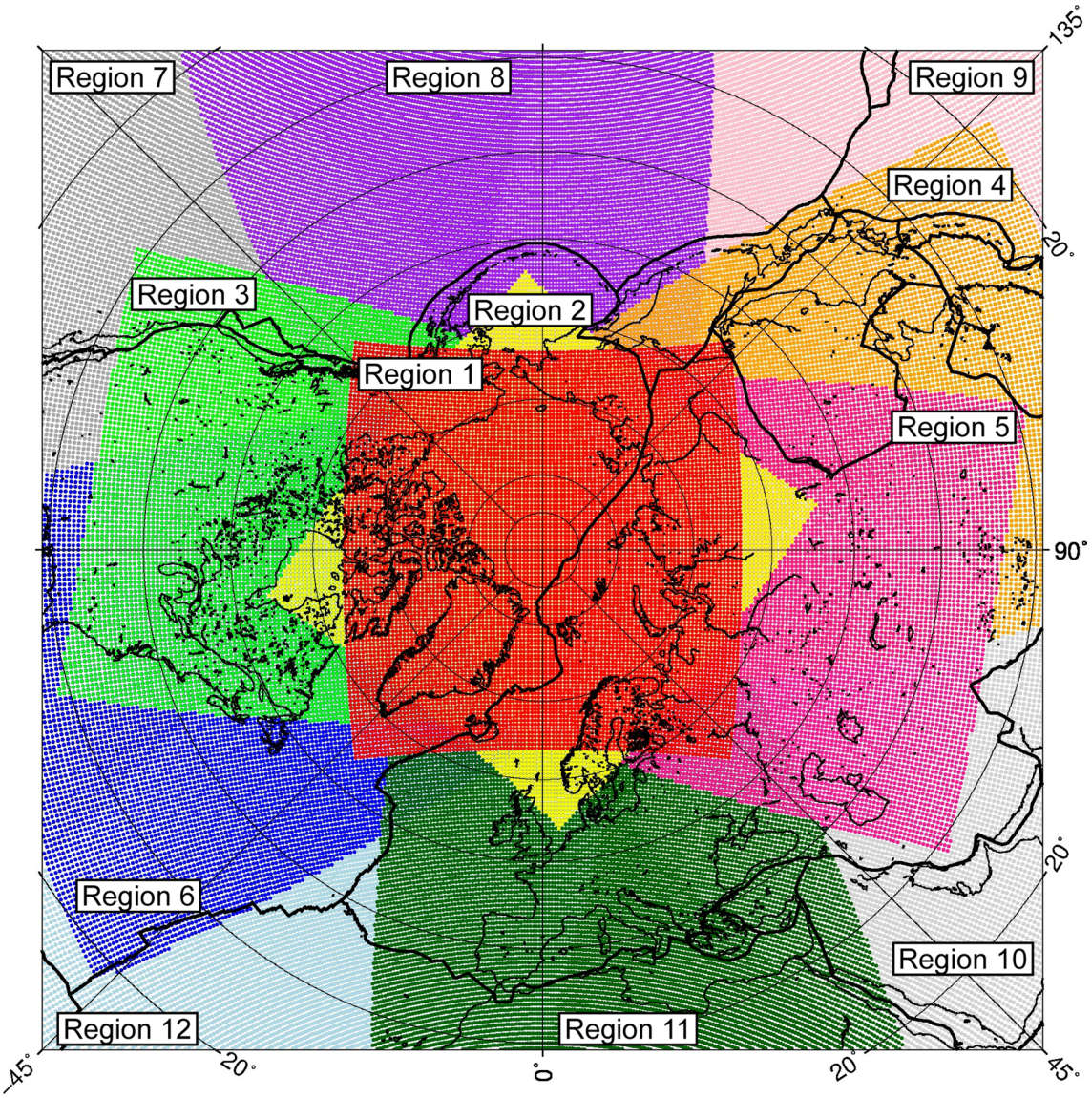

Fig. 3 Distribution of Regions 1–12 listed in Table 1. The points denote the grid nodes adopted for interpolation to obtain the final tomographic model

to 120° and the latitude range from − 30° to 30° after the coordinate transformation. In the vicinity of the North Pole, where only a few seismic stations and earthquakes exist, calculations are performed in two regions rotated by ~ 40° around the North Pole to reduce the distortion of the tomographic results due to the grid arrangement (Regions 1 and 2). In addition, 10 regions with different positions and angles are further arranged around them (Regions 3–12) (Fig. 3).

Data are collected from the ISC-EHB catalog at the International Seismological Centre (ISC) website (http://www.isc.ac.uk/) and further selected for our analysis. The *P*, *pP*, and *PP* (Additional file 1: Fig. S1) arrival times from 170,435 earthquakes that occurred during 1964–2016 are selected. To make the hypocentral distribution uniform, the entire crust and mantle are divided into small cubic blocks, and in each block only one earthquake with the maximum number of data is extracted. We extract as many earthquakes as possible that occurred inside the target region, by adopting finer blocks inside the target region and coarser blocks outside it. The block size is changed for each calculation to roughly homogenize the number of earthquakes and data used in each calculation ("Block size" in Table 1 and Figs. 4 and Additional file 1: S2–S12). Table 1 also shows the numbers of earthquakes, seismic stations, and arrival time data used.

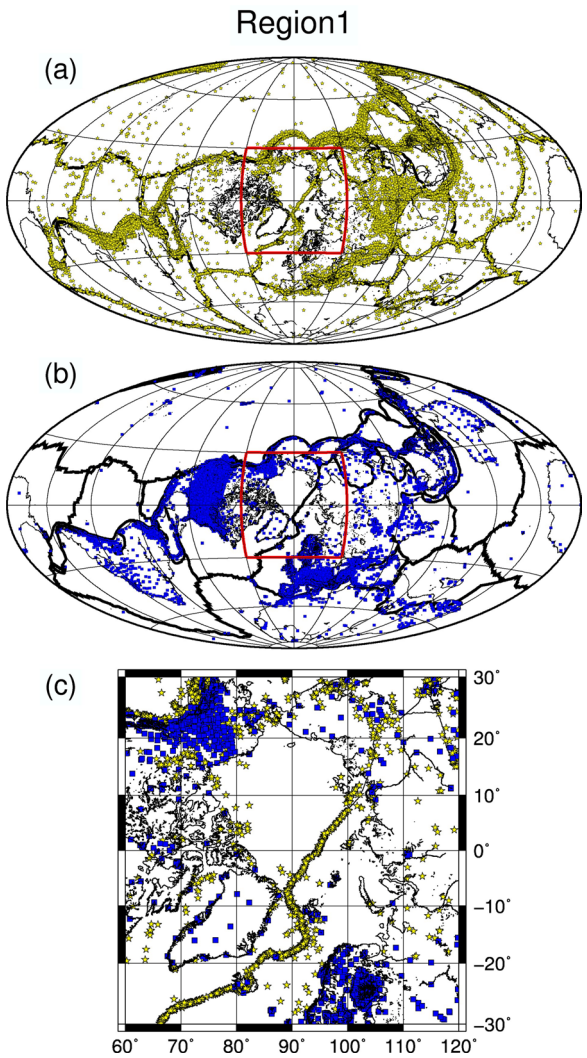

Fig. 4 Global distribution of **a** earthquakes and **b** seismic stations, and **c** distribution of earthquakes (yellow stars) and seismic stations (blue rectangles) inside the target region, used in the tomographic inversion for Region 1 (Table 1). The red box indicates the target region. The thick black lines denote plate boundaries. The coordinate transformation is applied (see the text for details)

We set up a fine 3-D grid with a lateral grid interval of 55.6 km (i.e., a great circle distance of 0.5° on the surface) in the target volume, and a coarse 3-D grid with a lateral grid interval of 222.39 km (a great circle distance of 2.0° on the surface) in the whole crust and mantle. The vertical grid intervals inside and outside the target volume are also different. Table S1 in the Additional file 1 shows the depths of grid meshes and the number of grid nodes at each depth inside and outside of the target volume. We note that theoretical travel times and ray paths are calculated using a 3-D ray tracing method (Zhao 2004) that combines the pseudo-bending scheme (Um and Thurber 1987) and Snell's law. The IASP91 model (Kennett and Engdahl 1991) is taken to be the 1-D initial V_P model for the tomographic inversion (Additional file 1: Fig. S13). The LSQR algorithm (Paige and Saunders 1982) with damping and smoothing regularizations is used to conduct the tomographic inversion (Zhao 2004). The optimal values of the damping and smoothing parameters are determined by conducting trade-off curve analysis following the previous studies (Toyokuni et al. 2020b, 2022; Zhao et al. 2017, 2021).

The obtained 12 tomographic models are combined with the following procedure (Additional file 1: Fig. S14).

1. To reduce the boundary effect of the target region, the edges of each tomographic model are cut off. Considering the trade-off between the degree of smooth connection among regions and the amount of information, we extract only the results 4° inside the longitude and latitude ranges of each target region.
2. Transforming the coordinates of the 12 tomographic models and aligning them with the coordinate system of Region 1.
3. A grid for connection (hereinafter we call it connection grid) is generated with an interval of 0.5° in both latitude and longitude directions and an interval of 10 km in depth direction from the surface to the core-mantle boundary (CMB) according to the coordinate system of Region 1.
4. Finding the V_P and ray hit-count values of each tomographic model at the connection grid. This is done by linear interpolation of the values at the eight grid nodes of each tomographic model surrounding the connection grid.
5. At the connection grid, weighted average of overlapping tomographic models is performed using the ray hit-count.

As a result, the final tomographic model is obtained from the surface to the CMB beneath the region north of ~ 30°N latitude. Such jointing of multiple tomographic models has been adopted by previous studies targeting a wide area (e.g., Jakovlev et al. 2012). Figure 5 shows the transition of the tomographic result when the number of regions is gradually increased from the result when only Region 1 is considered. Even after more regions are added, the fluctuation of the structural features is negligible, and no artificial structural boundary appears.

The edge cutoff width (4°) in the above-mentioned step (1) is selected based on the following results. Figure

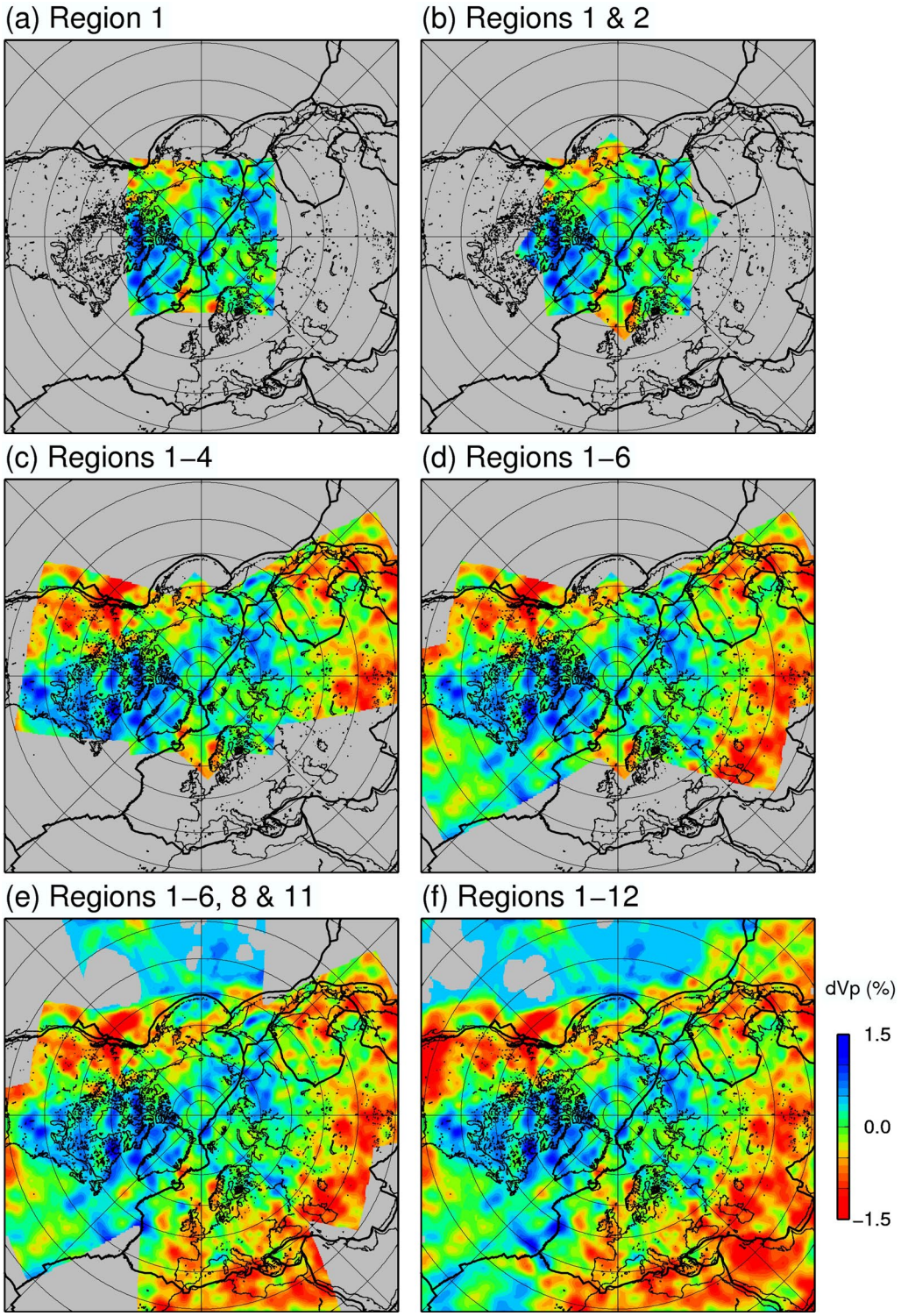

Fig. 5 Map views of V_P tomography at a depth of 800 km for **a** Region 1 only, **b** Regions 1 and 2, **c** Regions 1–4, **d** Regions 1–6, **e** Regions 1–6, 8, and 11, and **f** Regions 1–12. The blue and red colors denote high and low V_P perturbations, respectively, whose scale (in %) is shown on the right. Areas with average hit counts < 20 are masked in gray. Thick black lines: plate boundaries

S15 in the Additional file 1 shows the difference in the connection results due to different edge cutoff widths for each of the 12 inversion regions for a vertical cross-section through North America. Six results are shown: without the edge cutoff, and with the edge cutoff widths of 1°, 2°, 3°, 4°, and 5°. As for this cross-section, when the edge cutoff width is 3° or smaller, the influence of the edges of each tomographic model on the inversion regions is clearly visible. However, when the edge cutoff width is 4° or 5°, the connection looks smooth. To demonstrate this more objectively, we performed the following analysis. For each connection grid, we calculate the difference in V_P perturbations (dV_P) for each of the connected results without the edge cutoff, and with the edge cutoff widths of 1°, 2°, 3°, and 4°, from the reference result with the edge cutoff width of 5°. The arithmetic mean roughness (AMR) of the differences is calculated as follows:

$$AMR_i(\%) = \frac{1}{N}\sum_{n=1}^{N}\left|dV_{Pin} - dV_{P5n}\right| \quad (1)$$

where $i \in \{0, 1, 2, 3, 4\}$, N is the number of connection grid nodes within a range of ±2.5° from the boundaries of the inversion regions and with the ray hit-count ≥ 20, dV_{P0n} is dV_P of the connected tomographic model without edge cutoff at the nth grid, and dV_{Pin} is dV_P of the connected tomographic model with the edge cutoff width of i° at the nth grid. The resulting AMR_0, AMR_1, AMR_2, AMR_3, and AMR_4 are 0.0324, 0.0253, 0.0197, 0.0125, and 0.0070, respectively. We can see that as the edge cutoff width increases, the discrepancy across the boundaries between the inversion regions is reduced. Since there is almost no difference in the results for the edge cutoff widths of 4° and 5°, we adopt 4° as the cutoff width for the final model, considering the trade-off between the degree of smooth connection among the inversion regions and the amount of information.

The resolution of the tomographic images and the reliability of the obtained structural features are investigated by performing multiple synthetic tests including the checkerboard resolution test (CRT) (Humphreys and Clayton 1988; Zhao et al. 2017), restoring resolution test (RRT) (Toyokuni et al. 2021b; Zhao et al. 2017), and synthetic resolution test (SRT).

3 Results

Figure 6 shows selected map views of the tomographic image; the complete results are shown in the supporting information (Additional file 1: Fig. S16). For the areas where some of the 12 regions overlap, the ray hit count (HC) in each region is averaged, and the areas where average HC < 20 (Additional file 1: Fig. S17) are masked in white. At 160 km depth, high-V_P anomalies are visible in subduction zones (Marker A, Fig. 6a), and low-V_P (Marker B, Fig. 6a) and high-V_P (Marker C, Fig. 6a) anomalies appear in the western and eastern parts of North America, respectively, which are generally consistent with previous tomographic models (e.g., Golos et al. 2018). At 400 km depth, a low-V_P zone beneath the Iceland (Marker D, Fig. 6b) and Azores (Marker E, Fig. 6b) hotspots is visible. At a depth of 800 km, a wide range of high-V_P from North America to North Eurasia (Marker F, Fig. 6c) and low-V_P in surrounding regions (Marker G, Fig. 6c) are prominent. At a depth of 1500 km, no distinctive feature is visible (Fig. 6d), but at 2100 km depth the "Greenland plume" (Marker H, Fig. 6e) (Toyokuni et al. 2020b) and low-V_P anomalies beneath the western Pacific (Marker I, Fig. 6e) are prominent. At a depth of 2880 km, there is a marked increase in the amplitude of high-V_P and low-V_P anomalies near the CMB (Fig. 6f).

Figure 7 shows selected vertical cross-sections of the tomographic model, in which the zones with dV_P exceeding + 0.25% are outlined. The subducting Farallon slab beneath the North American continent is clearly visible down to the lower mantle (Fig. 7a). Beneath the Eurasian continent, the Izanagi slab penetrating into the lower mantle is also clearly revealed (Fig. 7c). The shapes of the Farallon and Izanagi slabs in our tomographic model are almost the same as those predicted theoretically (Peng et al. 2021), so they can be identified easily. As a plate becomes thicker and heavier as it moves away from the ridge axis, it is likely to fall into the lower mantle after stagnating around the 660-km discontinuity. The penetration of the Farallon slab into the lower mantle has already been revealed by many tomographic studies (e.g., Grand et al. 1997; Schmid et al. 2002; Zhao 2004; Zhao et al. 2013). However, the deep penetration of the Izanagi slab was only predicted by studies based on mantle convection modeling (Peng et al. 2021). This is the first time that the deeply penetrating Izanagi slab is clearly imaged by seismic tomography. In Fig. 7a, we can also see a low-V_P anomaly, which appears to be a hot plume rising from the CMB below Hawaii toward the western coast of North America (e.g., Nelson and Grand 2018; Steinberger et al. 2019).

Beneath Canada and Greenland, located between the two penetrating slabs, a high-V_P anomaly lies at a depth of ~800 km (Fig. 7b). Although this high-V_P anomaly is visible almost near the surface at the western end, it deepens toward the east and extends with a total length of ~2500 km. This feature looks like a supersized stagnant

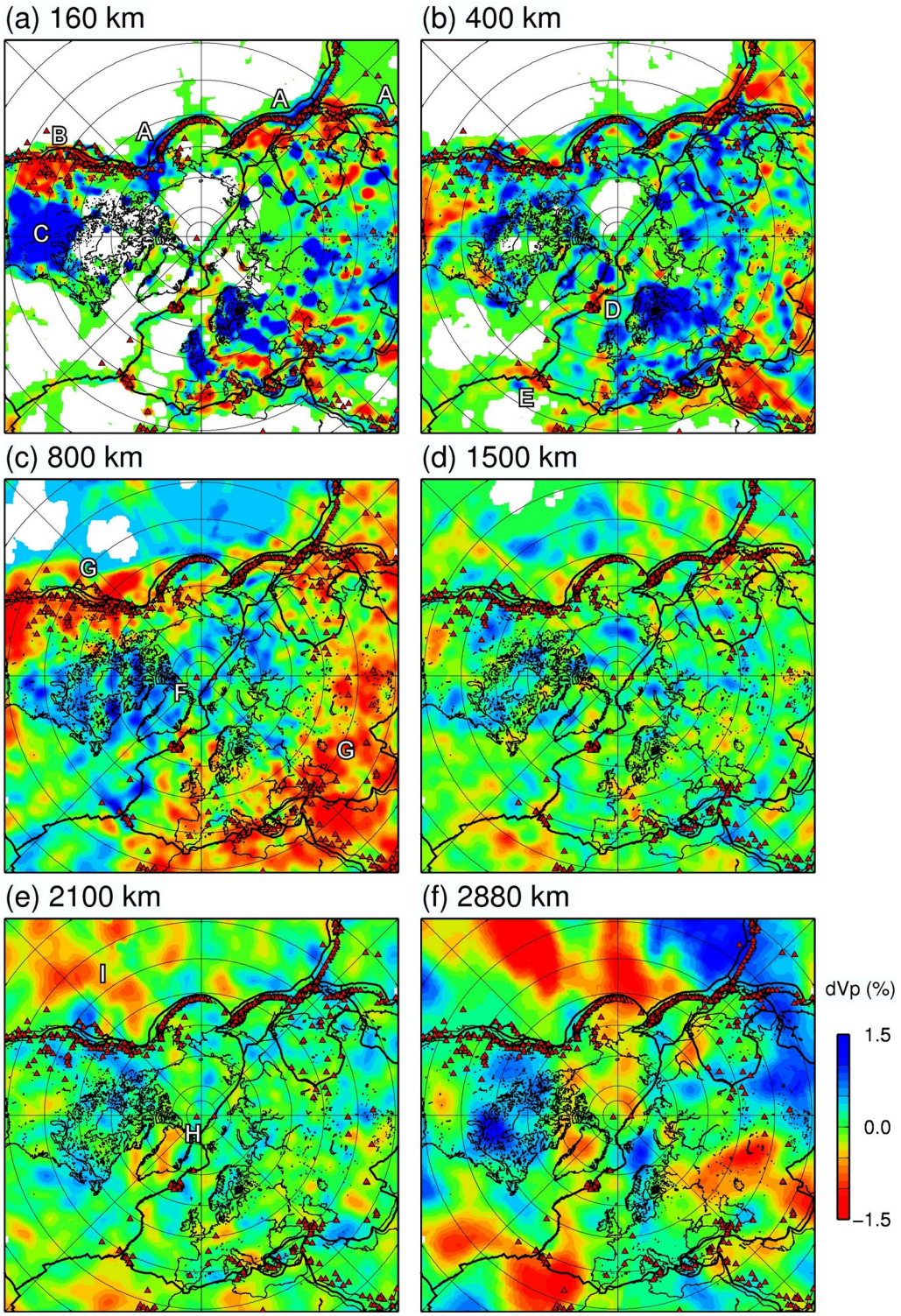

Fig. 6 Map views of V_P tomography at six depths obtained by this study. The layer depth is shown above each map. The blue and red colors denote high and low V_P perturbations, respectively, whose scale (in %) is shown on the right. Areas with average hit counts < 20 are masked in white. Red triangles: active volcanoes; thick black lines: plate boundaries

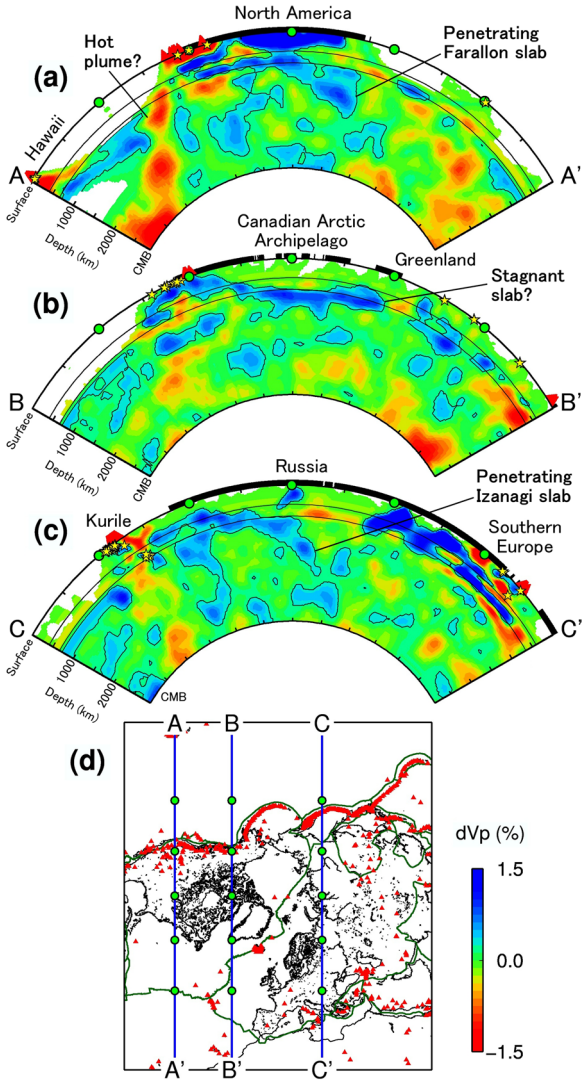

Fig. 7 Vertical cross-sections of V_P tomography showing main tectonic features. **a**–**c** Vertical cross-sections along three profiles as shown on the map **d**. The scale for V_P perturbation (in %) is shown on the bottom right. The 410-km and 660-km discontinuities are shown in black solid lines. The thick black lines on the surface denote land areas. Areas with average hit counts < 20 are masked in white. The blue zones outlined by thin black lines are high-V_P anomalies with amplitudes exceeding +0.25%. Red triangles: active volcanoes existing within ±2° of each profile; yellow stars: large earthquakes ($M \geq 6$) that occurred during 1964–2016 within ±2° of each profile; green circles: points dividing the section equidistantly using the central angle of the earth, which correspond to those in **d**. On the map (**d**), red triangles: active volcanoes; thick green lines: plate boundaries

slab. Vertical cross-sections with a finer grid interval beneath Canada and Greenland are shown in Fig. 8; the same cross-sections with a much finer grid interval are shown in the supporting information (Additional file 1: Fig. S18). The appearance changes even in a narrow area, but the high-V_P anomaly dipping eastward down to the mantle transition zone (MTZ) beneath the west coast of the North American continent and lying long below the MTZ is visible in many cross-sections.

We compare our model with the previous global tomography models. Ten V_P tomographic models are adopted for the comparison, i.e., UU-P07 (Amaru 2007), MITP08 (Li et al. 2008), GyPSuM-P (Simmons et al. 2010), LLNL_G3Dv3 (Simmons et al. 2012), GAP-P4 (Fukao and Obayashi 2013; Obayashi et al. 2013), SPani-P (Tesoniero et al. 2015), Hosseini2016 (Hosseini 2016), MITP_USA_2016MAY (Burdick et al. 2017), TX2019slab-P (Lu et al. 2019), and DETOX-P3 (Hosseini et al. 2020). These models were downloaded from the SubMachine website (http://www.earth.ox.ac.uk/~smachine/cgi/index.php) (Hosseini et al. 2018). We compare our model with these previous models (Figs. 9, 10). Note that our model is displayed with a different color palette from that used in Figs. 5, 6, 7 and 8 to compare these models using the same color palette. These figures show that the main features in Fig. 7a are robust (A-A′ in Fig. 9), but those in Figs. 7b, c vary depending on the model (B-B′ in Fig. 9 and C-C′ in Fig. 10). Images of the Japan subduction zone are also shown in Fig. 10 (D-D′) for comparison with other models. The 3-D seismic structure under the Japan Islands is relatively well known, thanks to many previous studies of this region (see a recent review by Zhao 2021). Our model clearly shows the subducting Pacific slab, demonstrating the reliability of our V_P model.

To perform the resolution tests including CRT, RRT, and SRT, we construct the following five input V_P models: (1) CRT1: the checkerboard has a lateral grid interval of 278 km (a great circle distance of 2.5° on the surface) inside the study region, (2) CRT2: the lateral grid interval is 167 km (a great circle distance of 1.5° on the surface) inside the study region, (3) RRT1: highlighting the pattern of the obtained tomographic result, (4) RRT2: the same as RRT1 but a regional rectangular high-V_P anomaly is added at depths of 650–800 km, and (5) SRT: a regional rectangular high-V_P anomaly is added at depths of 0–250 km, but V_P perturbations at the other grid nodes are set to zero.

Main features of the test results are summarized in Figs. 11 and 12; the complete test results are shown in the supporting information for the CRT1 (Additional file 1: Fig. S19), CRT2 (Additional file 1: Fig. S20), RRT1 (Additional file 1: Fig. S21), RRT2 (Additional file 1: Fig. S22), and SRT (Additional file 1: Fig. S23). Figures S19 and S20 in the Additional file 1 show the distribution of recovery rates estimated from the CRT results:

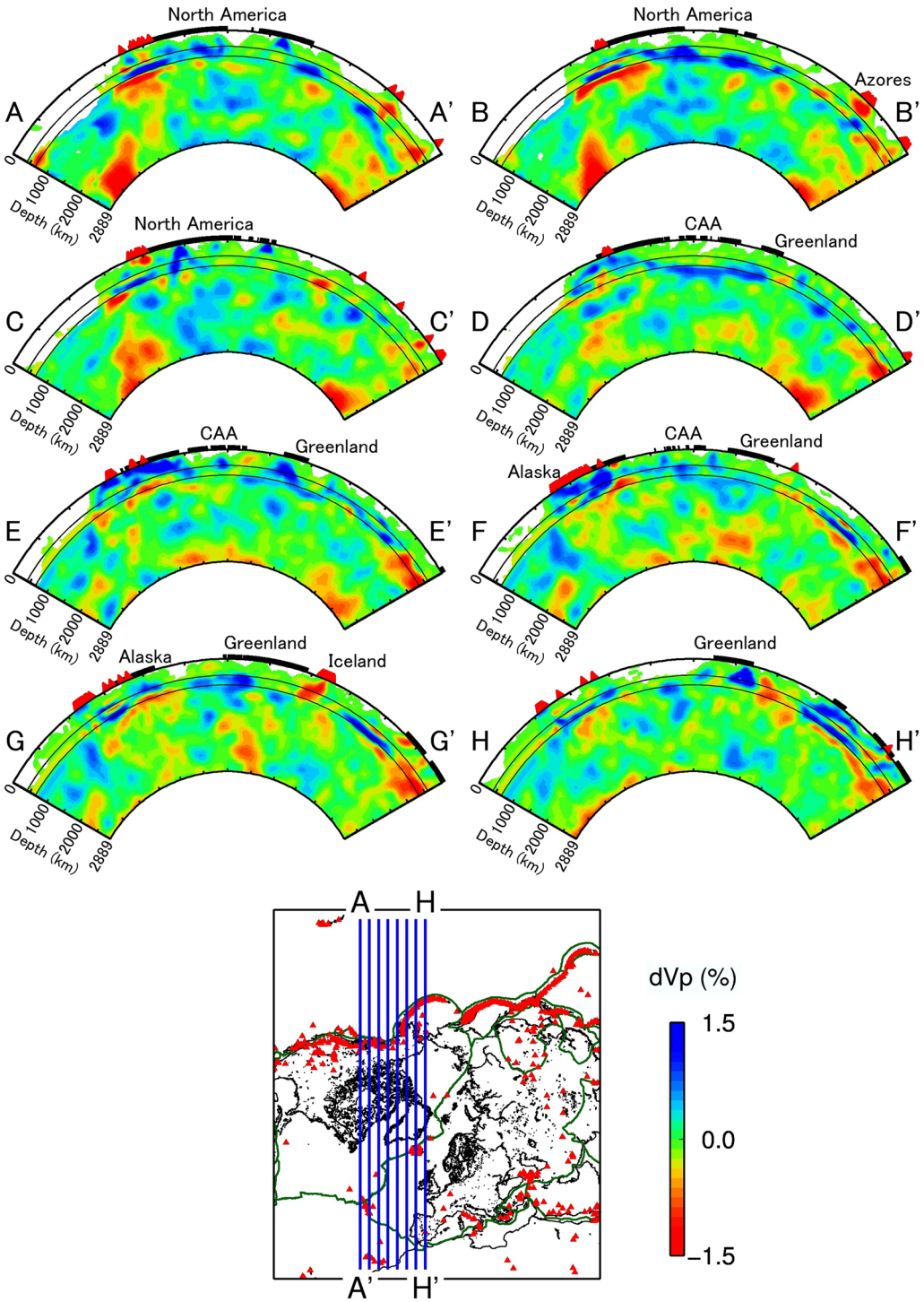

Fig. 8 Vertical cross-sections of V_P tomography along eight profiles beneath North America and Greenland as shown on the inset map. The 410-km and 660-km discontinuities are shown in black solid lines. The thick black lines on the surface denote land areas. Active volcanoes within a ±2° width of each profile are shown as red triangles. The color scale and masking threshold are the same as those in Fig. 7. CAA = Canadian Arctic Archipelago

$$RR_i(\%) = \frac{(dV_P \text{ at the } i\text{th node of the output model})}{(dV_P \text{ at the } i\text{th node of the input model})} \times 100 \quad (2)$$

The CRT results show that the resolution in our study region is 1.5° in the lateral direction and the distances comparable to the vertical grid interval in the depth direction for regions with average HC ≥ 20. The two RRT results (Figs. 11, Additional file 1: S21 and S22) show that the pattern of tomographic results can be recovered very well. The SRT results (Additional file 1: Fig. S23) show that our tomography does not have enough sensitivity to a high-V_P shallow craton (the upper 250 km depth) beneath the Canadian Shield, and that these shield anomalies are unlikely to be mistakenly imaged into the MTZ but in the shallow mantle as artificial velocity anomalies. Figure 12 shows the reliability of main features in Fig. 7.

4 Discussion

The map views at depths of ~700–800 km (Figs. 6c, 13e, f) show that the amplitude of high-V_P anomalies in the region from Canada to the Arctic Ocean is not uniform, and that the amplitude changes like stripes. Comparison of RRT1 and RRT2 results indicates that this feature is reliable (Fig. 11). By overlapping the results of plate reconstruction (Müller et al. 2019) according to a relationship between depth and subducted slab age (Butterworth et al. 2014), we can see that these stripes are coincident with the oceanic ridge axis subducted approximately normal to the trench axis. Specifically, the regions with the lineament of weaker high-V_P amplitudes are consistent well with the ridge axis between the Farallon and Kula plates subducted during ~60–50 Ma (Figs. 13d, e, f). Therefore, we consider that the lineament of weak high-V_P anomalies indicates the subducted oceanic ridge where the slab is thin, and the lineament with strong high-V_P zones on its both sides indicates the part where the slab is relatively thick. This correspondence reinforces the possibility that the high-V_P anomaly beneath this region reflects a stagnant slab.

According to Domeier et al. (2017), the previously considered Kula plate is a complex of the western Kronos plate and the eastern Kula plate, with subduction of the Kula plate beneath the Kronos plate forming a westward slope. In this case, the subduction axis of the Kula plate runs almost parallel to the eastern Kula–Farallon ridge, which better corresponds to the two parallel lineaments of weak high-V_P zones beneath North America in our tomographic results.

The plate near the ridge axis is young and less heavy, so it is easy to stagnate at a depth in the mantle. Furthermore, the trench axis due to the subduction of this area continued to retreat (Fig. 13), providing an environment where the slab stagnation was likely to occur. When the slab is light enough, it does not fall into the lower mantle but keeps stagnating until it is thermally assimilated with its surroundings (Nakakuki et al. 2010).

Above the long stagnant slab, a broad wedge-shaped mantle called the Big Mantle Wedge (BMW) is formed, which was firstly found in East Asia (Zhao et al. 2004, 2009; Lei and Zhao 2005). In the BMW, subduction-driven corner flow and fluids from deep dehydration reactions of the stagnant Pacific slab in the MTZ result in upwelling of hot and wet asthenospheric materials, causing the Japan Sea opening, intraplate volcanism and continental rift systems in East Asia. The BMW above the subducted Farallon/Nazca slab also caused Cenozoic intraplate magmatism in Patagonia (Navarrete et al. 2020). Referring to these previous studies, combining our tomography and the plate reconstruction results, we propose that the BMW above the stagnant slab in the circum-Arctic region caused the continental breakup during ERE and the accompanying volcanism in West Greenland, Davis Strait, and Baffin Island in Tertiary.

Unlike East Asia and Patagonia, the stagnant slab in the present study region is characterized by the oceanic ridge axis subducted nearly normal to the trench axis. Because the oceanic plates diverge to both sides of the ridge axis, when the ridge is subducted, a tensional stress field is likely to form in the trench-parallel direction in the overlying plate. Combined with the dominant trench-normal tensional stress regime formed by upwelling flows in the BMW, the upper plate in this area is likely to be dominated by tensional stresses oriented in various directions, which might have induced the complex division of CAA (Fig. 14).

(See figure on next page.)

Fig. 9 Comparison of tomographic models along **A-A'** (upper, the same cross-section as Fig. 7a) and **B-B'** (lower, the same cross-section as Fig. 7b) profiles on the inset map. **a** This study, **b** GyPSuM-P (Simmons et al. 2010), **c** GAP-P4 (Fukao and Obayashi 2013; Obayashi et al. 2013), **d** LLNL_G3Dv3 (Simmons et al. 2012), **e** UU-P07 (Amaru 2007), **f** MITP08 (Li et al. 2008), **g** Hosseini2016 (Hosseini 2016), **h** SPani-P (Tesoniero et al. 2015), **i** MITP_USA_2016MAY (Burdick et al. 2017), **j** DETOX-P3 (Hosseini et al. 2020), and **k** TX2019slab-P (Lu et al. 2019). The same color scale is adopted for all models. The cross-sections **b**–**k** are generated at the SubMachine website (https://www.earth.ox.ac.uk/~smachine/cgi/index.php) (Hosseini et al. 2018)

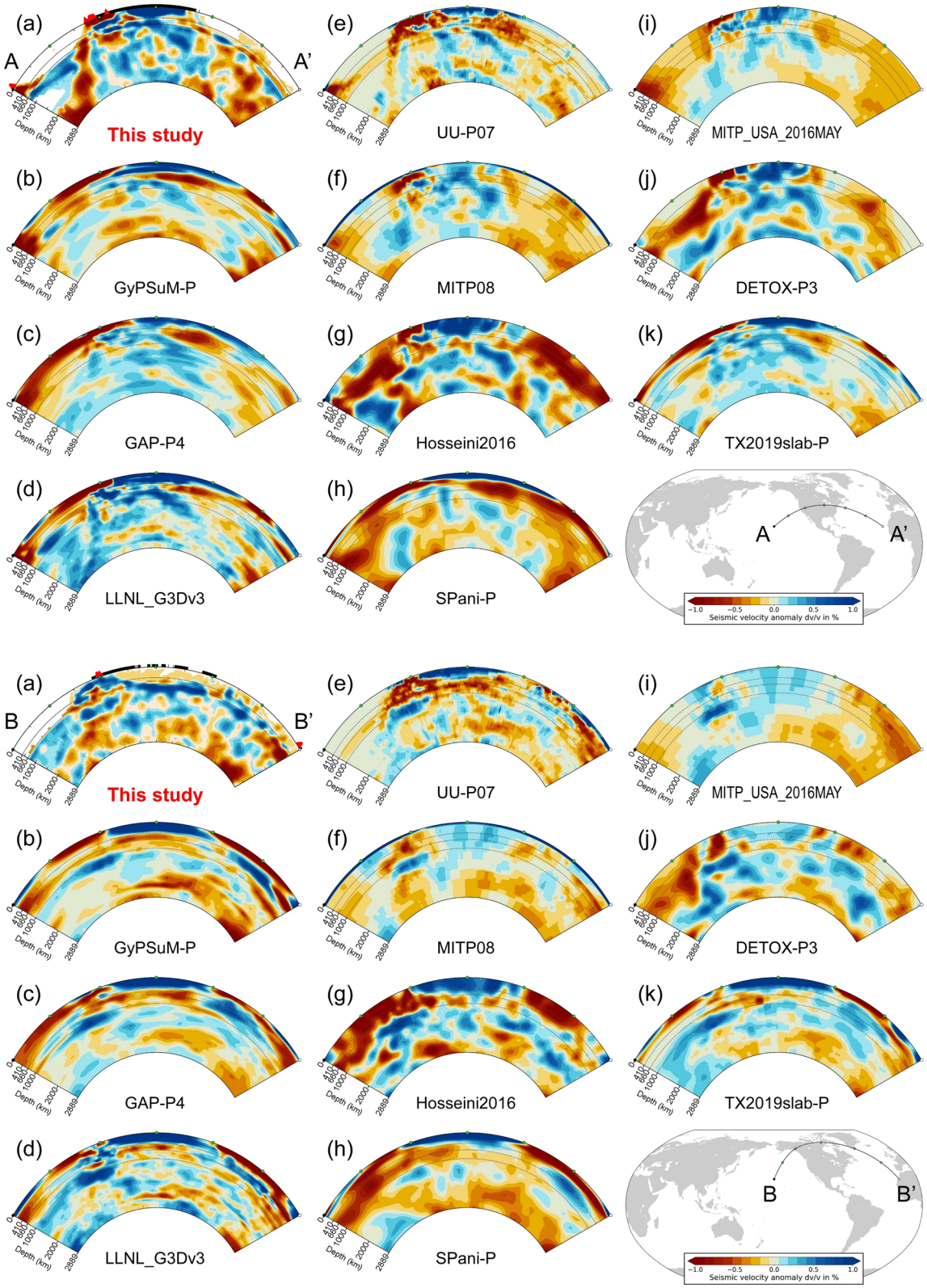

Fig. 9 (See legend on previous page.)

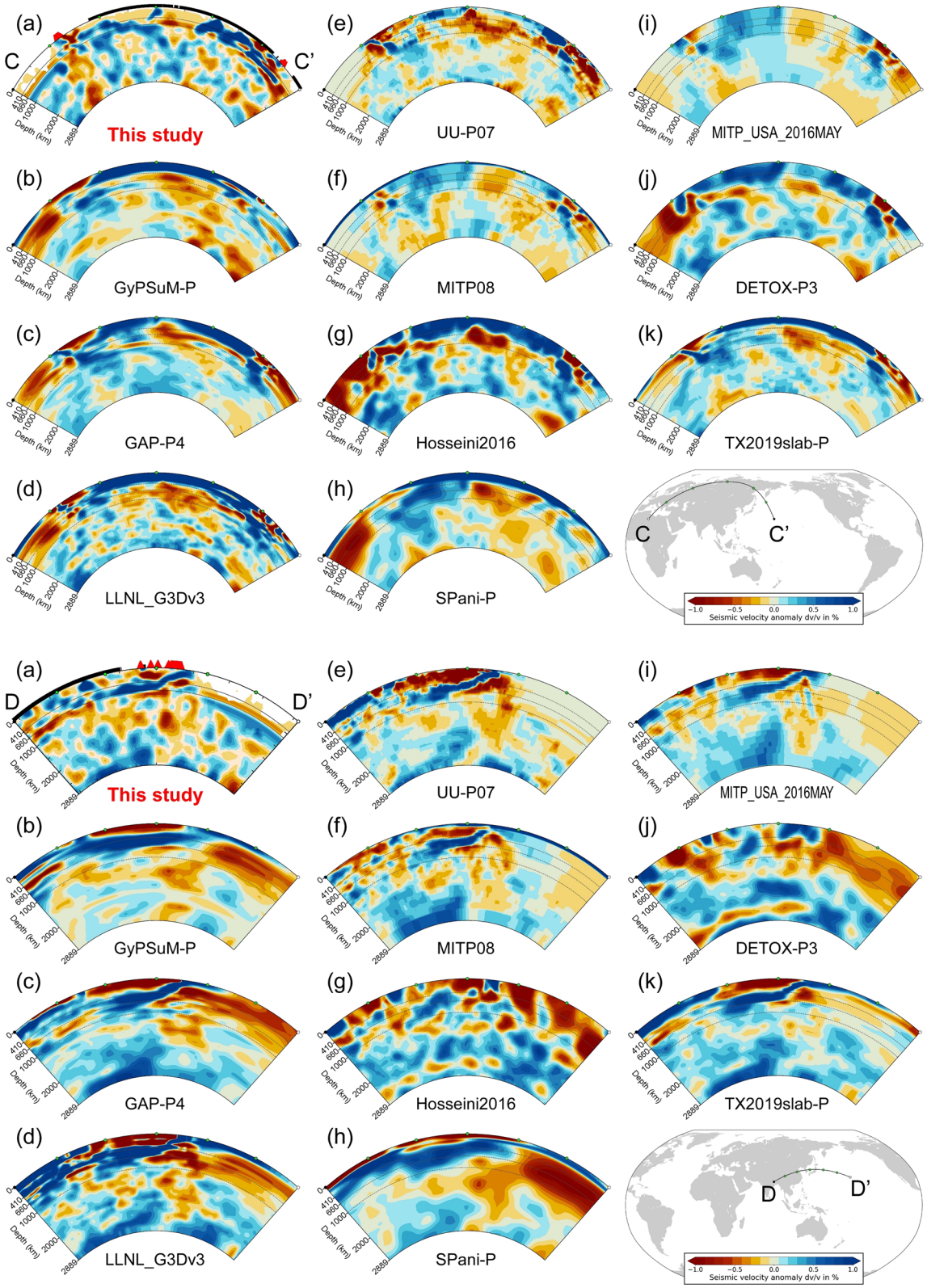

Fig. 10 The same as Fig. 9 but along **C–C′** (upper, the same cross-section as Fig. 7c) and **D**–**D′** (lower, a cross-section through the Japan subduction zone) profiles on the inset map

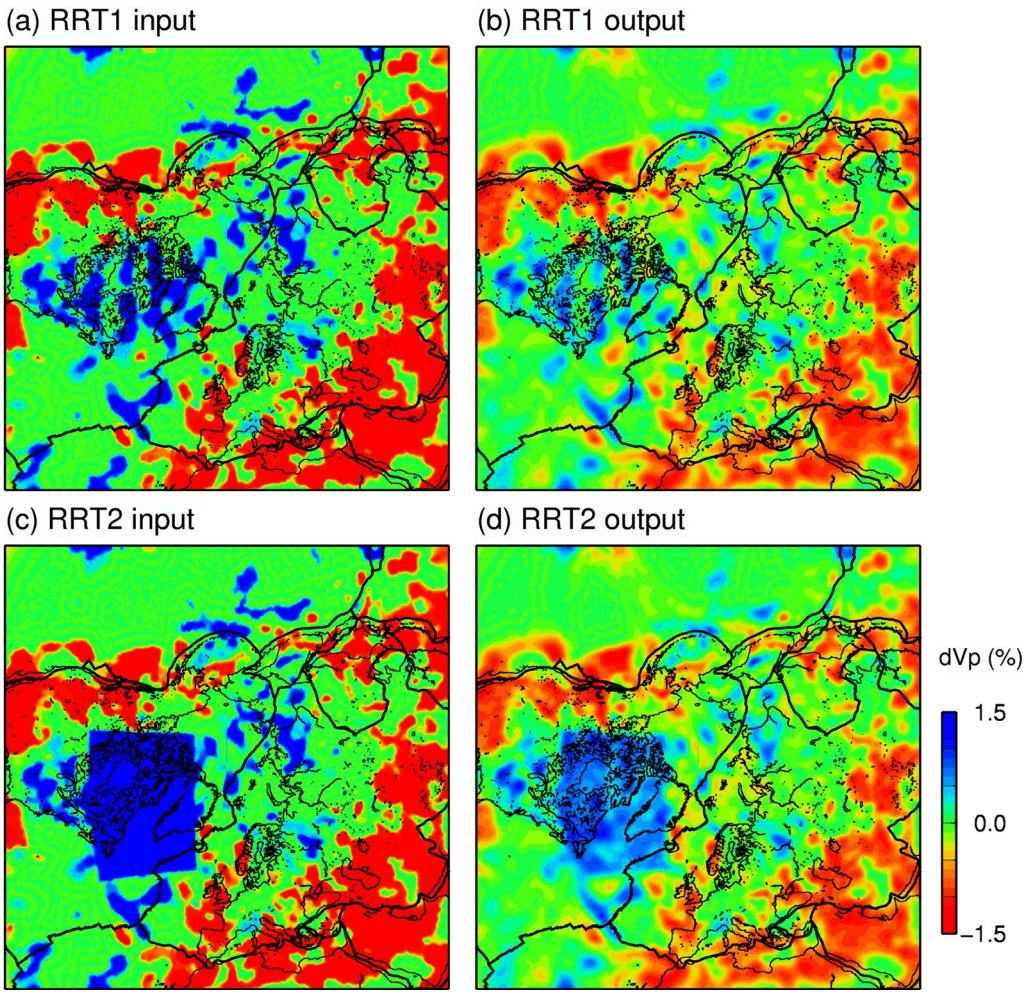

Fig. 11 Comparison of the RRT results at a depth of 800 km. **a** The RRT1 input model, **b** the RRT1 output result, **c** the RRT2 input model, and **d** the RRT2 output result. The blue and red colors denote high and low V_P perturbations, respectively, whose scale (in %) is shown on the right. The thick black lines denote plate boundaries

The root of this stagnant slab is located between the Cascadia and Alaska subduction zones in North America, where currently only the strike-slip Queen Charlotte Fault exists, and the subduction has already ceased. After the ERE, CARS became inactive and the entire rift system is now moving as part of the North American Plate. This fact also supports our proposal that CARS was induced by the stagnant slab. Toyokuni et al. (2020b) discovered the Greenland plume ascending from the CMB beneath Greenland, which rises up eastward and is connected with Svalbard and Jan Mayen. The direction of plume trailing is opposite to the moving direction of the plate on which Greenland is placed. However, by considering that the stagnant slab may obstruct the upwelling flow, the unusual flowline of the Greenland plume (Toyokuni et al. 2020b) can be well explained.

A recent study of the Gakkel Ridge basalts suggested a subduction influence on the Gakkel MORB (Mid Ocean Ridge Basalt), which has a significant water enrichment compared to other MORBs sampled globally (Yang et al. 2021). These geochemical and lithological observations have higher spatial resolution around the Gakkel Ridge than our tomography, so it is hard to confirm one-to-one correspondence between the two results. However, our result shows that a stagnant slab exists near the Gakkel ridge, which supports the results of Yang et al. (2021).

The stagnant slab revealed by this study is a supersized one. Its flat portion in the mantle is as long as ~2000 km

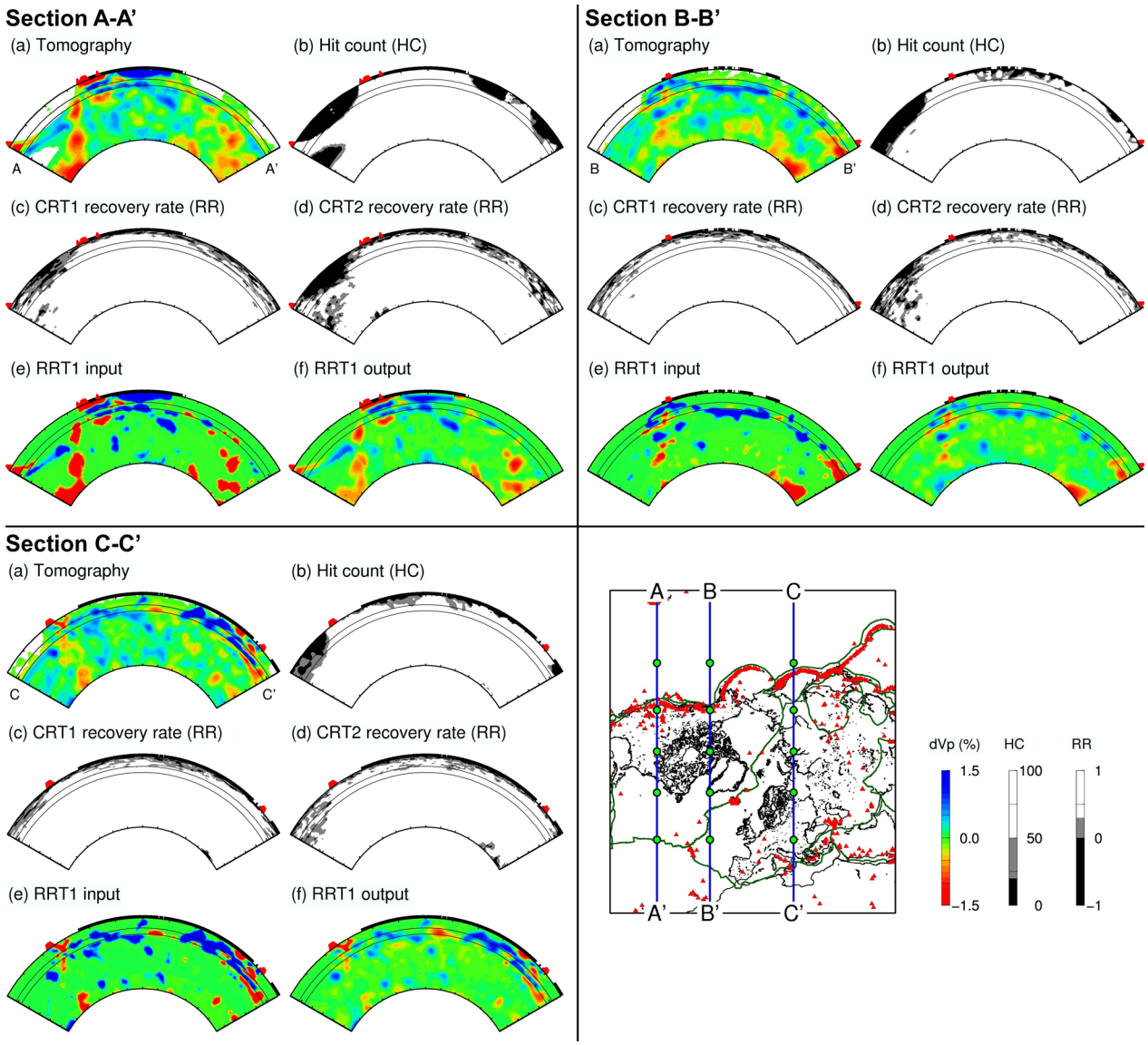

Fig. 12 Vertical cross-sections along **A–A′** (upper-left), **B–B′** (upper-right), and **C–C′** (lower-left) profiles on the inset map showing **a** the obtained tomographic model, **b** average ray hit count (HC), **c** recovery rate (RR) from the CRT1, **d** RR from the CRT2, **e** input model of RRT1, and **f** output result of RRT1. The color scales are shown beside the inset map. The 410-km and 660-km discontinuities are shown in black solid lines. The thick black lines on the surface denote land areas. The red triangles denote active volcanoes. On the inset map, red triangles: active volcanoes; thick green lines: plate boundaries

(Fig. 7b). Gianni et al. (2023) suggested that a similar supersized flat slab might exist beneath the Southern Atlantic–Southwest Indian ridges and provide MORBs with a residual subduction-related geochemical fingerprint. Our results suggest that a similar process might take place beneath the Arctic region. The persistence of such a stagnant slab depends on a variety of factors, including the slab age, trench retreat, and solid–solid phase transition within the slab (Faccenda and Dal Zilio 2017). Hence, further detailed studies are necessary to clarify this issue.

5 Conclusions

We investigate the detailed whole-mantle 3-D *P*-wave velocity (V_P) structure beneath the Northern Hemisphere north of 30°N latitude by combining detailed mantle tomographic models obtained piecewisely in 12 adjacent target regions. Our novel tomographic model reveals the following features.

1. The Farallon and Izanagi slabs subducting to the lower mantle are revealed clearly. In particular, the

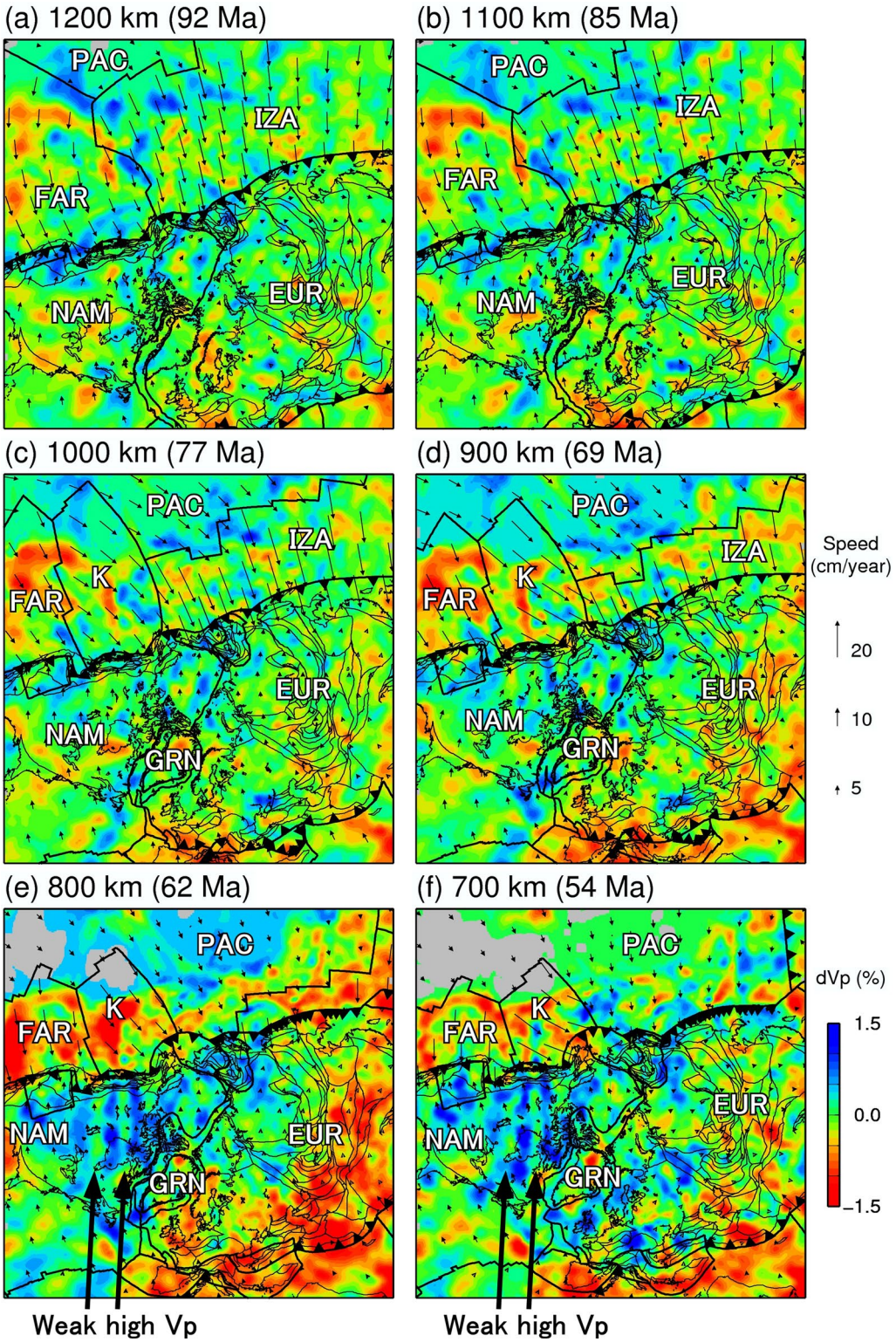

Fig. 13 Comparison of V_P map views obtained by this study with plate reconstructions (Müller et al. 2019) using an age-depth relationship (Butterworth et al. 2014). The depth of the tomography and the age of reconstruction are shown above each panel. The scale for V_P perturbation (in %) is shown on the right. In **e** and **f**, thick arrows show locations of weak high-V_P lineaments. Black jagged lines delineate subduction zones, and other black lines denote mid-ocean ridges and transform faults. The length and azimuth of each arrow denote the rate and direction of the absolute plate motion, respectively. The scale for the plate motion rate is shown on the right. EUR = Eurasian Plate; FAR = Farallon Plate; GRN = Greenland Plate; IZA = Izanagi Plate; K = Kula Plate; NAM = North American Plate; PAC = Pacific Plate

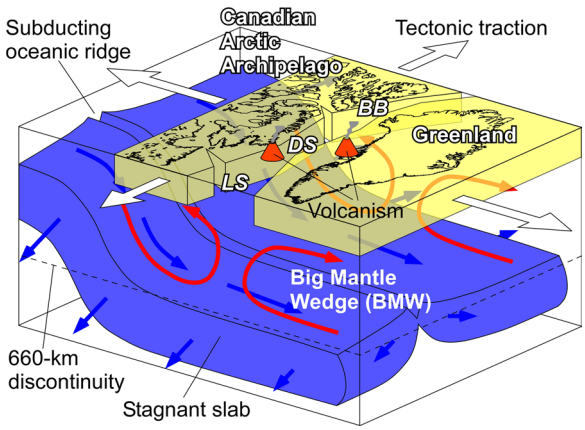

Fig. 14 Schematic diagram showing a possible mechanism of the division between Greenland and Canada and tearing of crust beneath the Canadian Arctic Archipelago revealed by this study. The subducting slab with oceanic ridge becomes stagnant below the 660-km discontinuity under Canada and Greenland. The red arrows indicate upwelling of hot asthenospheric materials due to convective circulation process in the Big Mantle Wedge. The blue arrows indicate subduction and divergence directions of the subducted slab. The white arrows on the surface indicate tectonic traction, whose length conceptually indicates the traction strength. BB = Baffin Bay; DS = Davis Strait; LS = Labrador Sea

position and shape of the Izanagi slab are clarified for the first time by this study.

2. A large-scale high-V_P body is revealed in and around the mantle transition zone beneath Arctic. Continuous subduction of young plates around the oceanic ridge that formed the boundary between the Farallon and Izanagi slabs might form a stagnant slab beneath this region, which is imaged as the high-V_P body. In addition, striped features perpendicular to the ancient trench appear in the high-V_P body, which may reflect the subducted oceanic ridges or boundaries of subducted microplates.
3. The subduction of the Farallon and Izanagi slabs and their stagnation might have resulted in a large-scale big mantle wedge (BMW) beneath the Arctic region, creating a tensional stress field in the overriding plate. These processes may have caused the breakup of Greenland and Canada followed by eruption of flood basalts and the formation of the Canadian Arctic Archipelago.

Abbreviations

AMR	Arithmetic mean roughness
BMW	Big mantle wedge
CAA	Canadian Arctic archipelago
CARS	Canadian Arctic rift system
CMB	Core-mantle boundary
CRT	Checkerboard resolution test
ERE	Eurekan rifting episode
HC	Hit count
MAR	Mid-Atlantic ridge
MORB	Mid ocean ridge basalt
MTZ	Mantle transition zone
RRT	Restoring resolution test
SRT	Synthetic resolution test

Supplementary Information

The online version contains supplementary material available at https://doi.org/10.1186/s40645-023-00595-7.

Additional file 1. Supporting information including 23 figures (Figs. S1–S23) and one table (Table S1).

Acknowledgements

We are grateful to Drs. Dean Childs, Kevin Nikolaus, Kent Anderson, Masaki Kanao, Yoko Tono, Seiji Tsuboi, Robin Abbott, Kathy Young, Drew Abbott, Silver Williams, Jason Hebert, Tetsuto Himeno, Susan Whitley, Orlando Leone, Akram Mostafanejad, Kirsten Arnell, and other staff members at GLISN, IRIS/PASSCAL, CH2M HILL Polar Services, and Norlandair for their contributions to the field operations in Greenland. Prof. Fenglin Niu (the Editor) and two anonymous referees provided thoughtful review comments and suggestions, which have improved this paper.

Author contributions

GT and DZ designed the study. DZ and GT developed the methodology. GT analyzed the data, visualized the results, and wrote the original draft that is improved by DZ. GT also installed and maintained six seismic stations on icecap and bedrock in Greenland used in this study. Both authors read and approved the final manuscript.

Funding

This work was partially supported by research grants from Japan Society for the Promotion of Science (Nos. 18K03794, 22K03749, 24403006, 23224012, 19H01996, and 26241010).

Availability of data and materials

The GMT (Wessel et al. 2013) and GPlates (Müller et al. 2018) software packages are used in this study. The SubMachine website (https://www.earth.ox.ac.uk/~smachine/cgi/index.php) (Hosseini et al. 2018) is used to generate cross-sections of other tomographic models. Arrival-time data are downloaded from the ISC-EHB database (http://www.isc.ac.uk/).

Declarations

Competing interests

The authors declare that they have no competing interest.

Received: 25 June 2023 Accepted: 22 October 2023
Published online: 08 November 2023

References

Amaru ML (2007) Global travel time tomography with 3-D reference models. Doctoral thesis, Utrecht University. https://dspace.library.uu.nl/handle/1874/314949

Antonijevic SK, Lees JM (2018) Effects of the Iceland plume on Greenland's lithosphere: new insights from ambient noise tomography. Polar Sci 17:75–82. https://doi.org/10.1016/j.polar.2018.06.004

Artemieva IM (2019) Lithosphere thermal thickness and geothermal heat flux in Greenland from a new thermal isostasy method. Earth Sci Rev 188:469–481. https://doi.org/10.1016/j.earscirev.2018.10.015

Burdick S, Vernon FL, Martynov V, Eakins J, Cox T, Tytell J, Mulder T, White MC, Astiz L, Pavlis GL, van der Hilst RD (2017) Model update May 2016: upper-mantle heterogeneity beneath North America from travel-time

tomography with global and USArray data. Seismol Res Lett 88(2A):319–325. https://doi.org/10.1785/0220160186
Butterworth NP, Talsma AS, Müller RD, Seton M, Bunge HP, Schuberth BSA, Shephard GE, Heine C (2014) Geological, tomographic, kinematic and geodynamic constraints on the dynamics of sinking slabs. J Geodyn 73:1–13. https://doi.org/10.1016/j.jog.2013.10.006
Chalmers JA, Larsen LM, Pedersen AK (1995) Widespread Palaeocene volcanism around the northern North Atlantic and Labrador Sea: evidence for a large, hot, early plume head. J Geol Soc 152:965–969. https://doi.org/10.1144/GSL.JGS.1995.152.01.14
Clinton JF, Nettles M, Walter F, Anderson K, Dahl-Jensen T, Giardini D, Govoni A, Hanka W, Lasocki S, Lee WS, McCormack D, Mykkeltveit S, Stutzmann E, Tsuboi S (2014) Seismic network in Greenland monitors Earth and ice system. Eos Trans AGU 95(2):13–14. https://doi.org/10.1002/2014EO020001
Dal Zilio L (2018) Subduction-driven earth machine. Nat Geosci 11:229. https://doi.org/10.1038/s41561-018-0102-z
Dal Zilio L, Faccenda M, Capitanio F (2018) The role of deep subduction in supercontinent breakup. Tectonophysics 746:312–324. https://doi.org/10.1016/j.tecto.2017.03.006
Darbyshire FA, Larsen TB, Mosegaard K, Dahl-Jensen T, Gudmundsson Ó, Bach T, Gregersen S, Pedersen HA, Hanka W (2004) A first detailed look at the Greenland lithosphere and upper mantle, using Rayleigh wave tomography. Geophys J Int 158(1):267–286. https://doi.org/10.1111/j.1365-246X.2004.02316.x
Darbyshire FA, Dahl-Jensen T, Larsen TB, Voss PH, Joyal G (2018) Crust and uppermost-mantle structure of Greenland and the Northwest Atlantic from Rayleigh wave group velocity tomography. Geophys J Int 212(3):1546–1569. https://doi.org/10.1093/gji/ggx479
Domeier M, Shephard GE, Jakob J, Gaina C, Doubrovine PV, Torsvik TH (2017) Intraoceanic subduction spanned the Pacific in the Late Cretaceous–Paleocene. Sci Adv 3(11):eaao2303. https://doi.org/10.1126/sciadv.aao2303
Faccenda M, Dal Zilio L (2017) The role of solid–solid phase transitions in mantle convection. Lithos 268–271:198–224. https://doi.org/10.1016/j.lithos.2016.11.007
Fukao Y, Obayashi M (2013) Subducted slabs stagnant above, penetrating through, and trapped below the 660 km discontinuity. J Geophys Res Solid Earth 118:5920–5938. https://doi.org/10.1002/2013JB010466
Gerlings J, Funck T, Jackson HR, Louden KE, Klingelhöfer F (2009) Seismic evidence for plume-derived volcanism during formation of the continental margin in southern Davis Strait and northern Labrador Sea. Geophys J Int 176:980–994. https://doi.org/10.1111/j.1365-246X.2008.04021.x
Gianni GM, Likerman J, Navarrete CR, Gianni CR, Zlotnik S (2023) Ghost-arc geochemical anomaly at a spreading ridge caused by supersized flat subduction. Nat Commun 14:2083. https://doi.org/10.1038/s41467-023-37799-w
Gill RCO, Pedersen AK, Larsen JG (1992) Tertiary picrites in West Greenland: melting at the periphery of a plume? In: Storey BC, Alabaster T, Pankhurst RJ (eds) Magmatism and the causes of continental break-up, vol 68. Geological Society of London, London, pp 335–348. https://doi.org/10.1144/GSL.SP.1992.068.01.21
Gion AM, Williams SE, Müller RD (2017) A reconstruction of the Eurekan Orogeny incorporating deformation constraints. Tectonics 36:304–320. https://doi.org/10.1002/2015TC004094
Golos EM, Fang H, Yao H, Zhang H, Burdick S, Vernon F, Schaeffer A, Lebedev S, van der Hilst RD (2018) Shear wave tomography beneath the United States using a joint inversion of surface and body waves. J Geophys Res Solid Earth 123:5169–5189. https://doi.org/10.1029/2017JB014894
Grand SP, van der Hilst RD, Widiyantoro S (1997) Global seismic tomography: a snapshot of convection in the Earth. GSA Today 7(4):1–7
Hosseini K (2016) Global multiple-frequency seismic tomography using teleseismic and core-diffracted body waves. Ph. D. Thesis, Faculty of Geosciences, LMU München. https://doi.org/10.5282/edoc.19597
Hosseini K, Matthews KJ, Sigloch K, Shephard GE, Domeier M, Tsekhmistrenko M (2018) SubMachine: web-based tools for exploring seismic tomography and other models of Earth's deep interior. Geochem Geophys Geosyst 19(5):1464–1483. https://doi.org/10.1029/2018GC007431
Hosseini K, Sigloch K, Tsekhmistrenko M, Zaheri A, Nissen-Meyer T, Igel H (2020) Global mantle structure from multifrequency tomography using *P*, *PP* and *P*-diffracted waves. Geophys J Int 220(1):96–141. https://doi.org/10.1093/gji/ggz394
Humphreys E, Clayton RW (1988) Adaptation of back projection tomography to seismic travel time problems. J Geophys Res 93:1073–1085. https://doi.org/10.1029/JB093iB02p01073
Jakovlev AV, Bushenkova NA, Koulakov IY, Dobretsov NL (2012) Structure of the upper mantle in the Circum-Arctic region from regional seismic tomography. Russ Geol Geophys 53(10):963–971. https://doi.org/10.1016/j.rgg.2012.08.001
Kennett BLN, Engdahl ER (1991) Traveltimes for global earthquake location and phase identification. Geophys J Int 105:429–465. https://doi.org/10.1111/j.1365-246X.1991.tb06724.x
Kumar P, Kind R, Priestley K, Dahl-Jensen T (2007) Crustal structure of Iceland and Greenland from receiver function studies. J Geophys Res Solid Earth 112(B3):B03301. https://doi.org/10.1029/2005JB003991
Larsen LM, Pedersen AK, Tegner C, Duncan RA, Hald N, Larsen JG (2016) Age of Tertiary volcanic rocks on the West Greenland continental margin: volcanic evolution and event correlation to other parts of the North Atlantic Igneous Province. Geol Mag 153:487–511. https://doi.org/10.1017/S0016756815000515
Lebedev S, Schaeffer AJ, Fullea J, Pease V (2018) Seismic tomography of the Arctic region: inferences for the thermal structure and evolution of the lithosphere. Geol Soc Spec Publ 460:419–440. https://doi.org/10.1144/SP460.10
Lei J, Zhao D (2005) *P*-wave tomography and origin of the Changbai intraplate volcano in Northeast Asia. Tectonophysics 397:281–295. https://doi.org/10.1016/j.tecto.2004.12.009
Levshin AL, Shen W, Barmin MP, Ritzwoller MH (2017) Surface wave studies of the Greenland upper lithosphere using ambient seismic noise. https://pdfs.semanticscholar.org/977c/ce2101b7f9b384d38e9b051bf289a7277b54.pdf
Li C, van der Hilst RD, Engdahl ER, Burdick S (2008) A new global model for *P* wave speed variations in Earth's mantle. Geochem Geophys Geosyst 9(5):Q05018. https://doi.org/10.1029/2007GC001806
Lu C, Grand SP, Lai H, Garnero EJ (2019) TX2019slab: A new *P* and *S* tomography model incorporating subducting slabs. J Geophys Res Solid Earth 124:11549–11567. https://doi.org/10.1029/2019JB017448
Martos YM, Jordan TA, Catalán M, Jordan TM, Bamber JL, Vaughan DG (2018) Geothermal heat flux reveals the Iceland hotspot track underneath Greenland. Geophys Res Lett 45:8214–8222. https://doi.org/10.1029/2018GL078289
Mordret A (2018) Uncovering the Iceland hot spot track beneath Greenland. J Geophys Res Solid Earth 123:4922–4941. https://doi.org/10.1029/2017JB015104
Mordret A, Mikesell TD, Harig C, Lipovsky BP, Prieto GA (2016) Monitoring southwest Greenland's ice sheet melt with ambient seismic noise. Sci Adv 2(5):e1501538. https://doi.org/10.1126/sciadv.1501538
Müller RD, Cannon J, Qin X, Watson RJ, Gurnis M, Williams S, Pfaffelmoser T, Seton M, Russell SHJ, Zahirovic S (2018) GPlates: building a virtual Earth through deep time. Geochem Geophys Geosyst 19:2243–2261. https://doi.org/10.1029/2018GC007584
Müller RD, Zahirovic S, Williams SE, Cannon J, Seton M, Bower DJ, Tetley MG, Heine C, Le Breton E, Liu S, Russell SHJ, Yang T, Leonard J, Gurnis M (2019) A global plate model including lithospheric deformation along major rifts and orogens since the Triassic. Tectonics 38(6):1884–1907. https://doi.org/10.1029/2018TC005462
Nakakuki T, Tagawa M, Iwase Y (2010) Dynamical mechanisms controlling formation and avalanche of a stagnant slab. Phys Earth Planet Inter 183:309–320. https://doi.org/10.1016/j.pepi.2010.02.003
Navarrete C, Gianni G, Massaferro G, Butler K (2020) The fate of the Farallon slab beneath Patagonia and its links to Cenozoic intraplate magmatism, marine transgressions and topographic uplift. Earth-Sci Rev 210:103379. https://doi.org/10.1016/j.earscirev.2020.103379
Nelson PL, Grand SP (2018) Lower-mantle plume beneath the Yellowstone hotspot revealed by core waves. Nat Geosci 11:280–284. https://doi.org/10.1038/s41561-018-0075-y
Obayashi M, Yoshimitsu J, Nolet G, Fukao Y, Shiobara H, Sugioka H, Miyamachi H, Gao Y (2013) Finite frequency whole mantle *P* wave tomography: improvement of subducted slab images. Geophys Res Lett 40:5652–5657. https://doi.org/10.1002/2013GL057401
Paige CC, Saunders MA (1982) LSQR, An algorithm for sparse linear equations and sparse least squares. ACM Trans Math Softw 8:43–71. https://doi.org/10.1145/355984.355989

Peace AL, Foulger GR, Schiffer C, McCaffrey KJ (2017) Evolution of Labrador Sea–Baffin Bay: plate or plume processes? Geosci Can 44(3):91–102. https://doi.org/10.12789/geocanj.2017.44.120

Peng D, Liu L, Wang Y (2021) A newly discovered Late-Cretaceous East Asian flat slab explains its unique lithospheric structure and tectonics. J Geophys Res Solid Earth 126:e2021JB022103. https://doi.org/10.1029/2021JB022103

Pilidou S, Priestley K, Gudmundsson Ó, Debayle E (2004) Upper mantle *S*-wave speed heterogeneity and anisotropy beneath the North Atlantic from regional surface wave tomography: the Iceland and Azores plumes. Geophys J Int 159:1057–1076. https://doi.org/10.1111/j.1365-246X.2004.02462.x

Pourpoint M, Anandakrishnan S, Ammon CJ, Alley RB (2018) Lithospheric structure of Greenland from ambient noise and earthquake surface wave tomography. J Geophys Res Solid Earth 123:7850–7876. https://doi.org/10.1029/2018JB015490

Rickers F, Fichtner A, Trampert J (2013) The Iceland–Jan Mayen plume system and its impact on mantle dynamics in the North Atlantic region: evidence from full-waveform inversion. Earth Planet Sci Lett 367:39–51. https://doi.org/10.1016/j.epsl.2013.02.022

Schmid C, Goes S, van der Lee S, Giardini D (2002) Fate of the Cenozoic Farallon slab from a comparison of kinematic thermal modeling with tomographic images. Earth Planet Sci Lett 204(1–2):17–32. https://doi.org/10.1016/S0012-821X(02)00985-8

Simmons NA, Forte AM, Boschi L, Grand SP (2010) GyPSuM: a joint tomographic model of mantle density and seismic wave speeds. J Geophys Res Solid Earth 115(B12):B12310. https://doi.org/10.1029/2010JB007631

Simmons NA, Myers SC, Johannesson G, Matzel E (2012) LLNL-G3Dv3: global P wave tomography model for improved regional and teleseismic travel time prediction. J Geophys Res Solid Earth 117:B10302. https://doi.org/10.1029/2012JB009525

Steinberger B, Nelson PL, Grand SP, Wang W (2019) Yellowstone plume conduit tilt caused by large-scale mantle flow. Geochem Geophys Geosyst 20:5896–5912. https://doi.org/10.1029/2019GC008490

Takenaka H, Komatsu M, Toyokuni G, Nakamura T, Okamoto T (2017) Quasi-Cartesian finite-difference computation of seismic wave propagation for a three-dimensional sub-global model. Earth Planets Space 69:67. https://doi.org/10.1186/s40623-017-0651-1

Tesoniero A, Auer L, Boschi L, Cammarano F (2015) Hydration of marginal basins and compositional variations within the continental lithospheric mantle inferred from a new global model of shear and compressional velocity. J Geophys Res Solid Earth 120:7789–7813. https://doi.org/10.1002/2015JB012026

Toyokuni G, Zhao D (2021) *P*-wave tomography for 3-D radial and azimuthal anisotropy beneath Greenland and surrounding regions. Earth Space Sci 8:e2021EA001800. https://doi.org/10.1029/2021EA001800

Toyokuni G, Kanao M, Tono Y, Himeno T, Tsuboi S, Childs D, Anderson K, Takenaka H (2014) Monitoring of the Greenland ice sheet using a broadband seismometer network: the GLISN project. Antarct Rec 58(1):1–18. https://doi.org/10.15094/00009722

Toyokuni G, Takenaka H, Kanao M, Tsuboi S, Tono Y (2015) Numerical modeling of seismic waves for estimating the influence of the Greenland ice sheet on observed seismograms. Polar Sci 9(1):80–93. https://doi.org/10.1016/j.polar.2014.12.001

Toyokuni G, Takenaka H, Takagi R, Kanao M, Tsuboi S, Tono Y, Childs D, Zhao D (2018) Changes in Greenland ice bed conditions inferred from seismology. Phys Earth Planet Inter 277:81–98. https://doi.org/10.1016/j.pepi.2017.10.010

Toyokuni G, Matsuno T, Zhao D (2020a) *P* wave tomography beneath Greenland and surrounding regions: 1. Crust and upper mantle. J Geophys Res Solid Earth 125:e2020JB019837. https://doi.org/10.1029/2020JB019837

Toyokuni G, Matsuno T, Zhao D (2020b) *P* wave tomography beneath Greenland and surrounding regions: 2. Lower mantle. J Geophys Res Solid Earth 125:e2020JB019839. https://doi.org/10.1029/2020JB0198379

Toyokuni G, Komatsu M, Takenaka H (2021a) Estimation of seismic attenuation of the Greenland Ice Sheet using 3-D waveform modeling. J Geophys Res Solid Earth 126:e2021JB021694. https://doi.org/10.1029/2021JB021694

Toyokuni G, Zhao D, Chen KH (2021b) Structural control on the 2018 and 2019 Hualien earthquakes in Taiwan. Phys Earth Planet Inter 312:106673. https://doi.org/10.1016/j.pepi.2021.106673

Toyokuni G, Zhao D, Kurata K (2022) Whole-mantle tomography of Southeast Asia: new insight into plumes and slabs. J Geophys Res Solid Earth 127:e2022JB024298. https://doi.org/10.1029/2022JB024298

Um J, Thurber C (1987) A fast algorithm for two-point seismic ray tracing. Bull Seismol Soc Am 77(3):972–986

Wessel P, Smith WHF, Scharroo R, Luis J, Wobbe F (2013) Generic Mapping Tools: improved version released. Eos Trans AGU 94(45):409–410. https://doi.org/10.1002/2013EO450001

Yang AY, Langmuir CH, Cai Y, Michael P, Goldstein SL, Chen Z (2021) A subduction influence on ocean ridge basalts outside the Pacific subduction shield. Nat Commun 12:4757. https://doi.org/10.1038/s41467-021-25027-2

Zhao D (2004) Global tomographic images of mantle plumes and subducting slabs: insight into deep Earth dynamics. Phys Earth Planet Inter 146:3–34. https://doi.org/10.1016/j.pepi.2003.07.032

Zhao D (2021) Seismic imaging of Northwest Pacific and East Asia: new insight into volcanism, seismogenesis and geodynamics. Earth Sci Rev 214:103507. https://doi.org/10.1016/j.earscirev.2021.103507

Zhao D, Lei J, Tang Y (2004) Origin of the Changbai intraplate volcanism in Northeast China: evidence from seismic tomography. Chin Sci Bull 49:1401–1408

Zhao D, Tian Y, Lei J, Liu L, Zheng S (2009) Seismic image and origin of the Changbai intraplate volcano in East Asia: role of big mantle wedge above the stagnant Pacific slab. Phys Earth Planet Inter 173:197–206. https://doi.org/10.1016/j.pepi.2008.11.009

Zhao D, Yamamoto Y, Yanada T (2013) Global mantle heterogeneity and its influence on teleseismic regional tomography. Gondwana Res 23:595–616. https://doi.org/10.1016/j.gr.2012.08.004

Zhao D, Fujisawa M, Toyokuni G (2017) Tomography of the subducting Pacific slab and the 2015 Bonin deepest earthquake (Mw 7.9). Sci Rep 7:44487. https://doi.org/10.1038/srep44487

Zhao D, Toyokuni G, Kurata K (2021) Deep mantle structure and origin of Cenozoic intraplate volcanoes in Indochina, Hainan and South China Sea. Geophys J Int 225:572–588. https://doi.org/10.1093/gji/ggaa605

Publisher's Note